Chemical Science

ROYAL SOCIETY OF CHEMISTRY

EDGE ARTICLE

View Article Online
View Journal

Cite this: DOI: 10.1039/d6sc02309f

All publication charges for this article have been paid for by the Royal Society of Chemistry

Promoting effect of nickel-chromium hydroxide on nickel phosphide nanosheets for efficient hydrogen production coupled with sulfion degradation

Xiaojun Wang,[a] Jieting Li,[a] Xinyu Zhu,[a] Zehua Xu,[a] Shuixiang Xie,[a] Shutong Chen,[a] Yuxuan Wan,[a] Guangyu Zhang,[a] Mingzheng Ge,[a] Wei Zhang,[a] Chao Wang *[b] and Rui-Qing Li *[a]

Received 20th March 2026
Accepted 28th April 2026

DOI: 10.1039/d6sc02309f

rsc.li/chemical-science

Electrochemical hydrogen production represents a sustainable approach for hydrogen generation. However, its large-scale practical application is largely limited by the sluggish oxygen evolution reaction (OER). In this study, the thermodynamically favorable sulfion oxidation reaction (SOR) is employed to replace the slow OER and nickel phosphide/nickel-chromium hydroxide ($Ni_2P/NiCr(OH)_2$) nanosheets are constructed to achieve low-energy hydrogen production. Benefiting from the interfacial water structure reorganization and electronic structure optimization caused by $NiCr(OH)_2$ introduction, and uniform nanosheet morphology, $Ni_2P/NiCr(OH)_2$ can achieve a current density of 10 mA cm^{-2} at low overpotentials for both the hydrogen evolution reaction and SOR. The assembled hybrid water electrolyzer requires small voltages of 0.513 and 0.698 V to reach 10 and 100 mA cm^{-2}, respectively, significantly lower than those of conventional water electrolysis. Moreover, $Ni_2P/NiCr(OH)_2$ exhibits excellent stability for 800 h at 200 mA cm^{-2} and realizes the conversion of sulfion into valuable elemental sulfur. This work presents a promising strategy for achieving energy-efficient hydrogen generation and resource utilization of sulfide-containing pollutants.

Introduction

In recent years, the continuous consumption of traditional fossil fuels has caused a series of serious environmental problems.[1] These problems include greenhouse gas emissions and air pollution. They have pushed researchers to speed up the research, development, and industrial application of renewable clean energy and related technologies.[2,3] Hydrogen (H_2) has high energy density, yields pollution-free combustion products, and has abundant raw material sources.[4,5] It is recognized as an ideal sustainable energy carrier to replace fossil fuels.[6] Hydrogen plays a pivotal role in alleviating energy demand pressure and constructing a clean energy ecosystem.[7,8] Currently, H_2 production pathways include fossil fuel-based H_2 production, industrial by-product H_2 recovery and water electrolysis.[9,10] Among them, water electrolysis technology with water as the raw material exhibits unique advantages and can produce high-purity green hydrogen with near-zero carbon emissions. It is a core hydrogen production technology integrating sustainability and environmental friendliness, and promoting the transformation of the energy structure.[11–13]

Water electrolysis typically involves the hydrogen evolution reaction (HER) at the cathode to directly produce hydrogen, and the oxygen evolution reaction (OER) at the anode with a standard potential as high as 1.23 V *vs.* the reversible hydrogen electrode (RHE).[14–16] Therefore, the OER with a high theoretical potential and sluggish kinetics results in substantial energy consumption is a major bottleneck of the overall water splitting (OWS) process. Specifically, actual anodic operating potentials are often significantly higher than 1.23 V due to limited mass transfer resistance, and ohmic polarization in practical electrolysis systems, further exacerbating the energy burden.[17–19] To overcome these limitations, replacing the OER with the oxidation of thermodynamically favorable small molecules has emerged as an attractive strategy.[20–23] This strategy not only effectively reduces the potentials of anodic reactions, but also enables the co-production of value-added chemicals and hydrogen.[24–26] Thereinto, the sulfide oxidation reaction (SOR, $S^{2-} \rightarrow S + 2e^-$) exhibits a lower standard potential of −0.48 V *vs.* RHE compared with the OER. Coupling the SOR with the HER in a hybrid water electrolyzer (HWE) can significantly reduce energy consumption of H_2 production. Furthermore, this strategy can convert sulfur-containing wastewater into valuable elemental sulfur under mild conditions, realizing resource utilization of pollutants, which provides a promising pathway for developing efficient and low-energy-consumption H_2 production.[27–29]

[a]School of Textile and Clothing, Nantong University, Nantong 226019, PR China. E-mail: liruiqing@ntu.edu.cn

[b]School of Chemistry and Chemical Engineering, Yangzhou University, Yangzhou 225002, China. E-mail: wangchao@yzu.edu.cn

Although metal-based electrocatalysts exhibit high catalytic activity for the SOR, the active metal sites are susceptible to corrosion and poisoning by S^{2-} when directly exposed to sulfur-containing electrolytes. This leads to the degradation of catalytic activity and stability. Therefore, developing catalysts with high activity and durability is imminent.[30–32] Transition metal phosphides (TMPs) have emerged as a research hotspot due to their advantages of good electrical conductivity, chemical corrosion resistance and compositional tunability. Over the past few decades, researchers have developed various synthetic methods including the hydrothermal method, phosphorization and electrodeposition method, to adjust morphology, electronic structures and reaction energy barriers of TMPs, which display good performances for the SOR and HER. For example, Shi *et al.* prepared the Mo–Pt–S composite catalyst *via* electroreduction and pulse electrodeposition methods, which exhibited excellent hydrogen evolution reaction performance with an overpotential of only 30.12 mV at a current density of 10 mA cm^{-2}.[33] Yu *et al.* fabricated the FeCoNiCrMn high-entropy alloy (HEA) *via* a two-step process of hydrothermal sulfurization followed by phosphorization. Endowed with abundant lattice defects and lattice strains, the as-prepared HEA exhibits remarkably superior electrocatalytic performance toward the SOR.[34] Liang *et al.* successfully synthesized a multiphase NiCoFe-based layered double hydroxide (NiCoFe-LDH) through a facile seed-assisted heterogeneous nucleation strategy. Featuring a unique micro-scale hydrangea-like morphology, the NiCoFe-LDH boasts an ultra-large specific surface area and synergistic active phases, which collectively provide abundant catalytic interfaces and reactive sites for the SOR.[35] Li *et al.* synthesized a Ni_3S_2/CoNiP material, which shows excellent catalytic performances for the HER, SOR, and nitrate reduction reaction (NO_3RR).[36] Even though some progress has been made, most exploited catalysts show monofunctional catalytic performances, which can lead to the deterioration and incompatibility of catalysts when pairing them in an electrolyzer. Therefore, developing bifunctional catalysts for the HER and SOR to realize efficient hydrogen production and sulfion upgradation is of utmost urgency.

In this work, Ni_2P/$NiCr(OH)_2$ nanosheets grown on nickel foam (NF) were successfully prepared *via* hydrothermal and low-temperature calcination methods. The experimental results indicate that the $NiCr(OH)_2$ introduction can reorganize the interfacial water structure and optimize the electronic structure of Ni_2P, which lead to improved catalytic performances of Ni_2P/$NiCr(OH)_2$ for both the HER and SOR. The integrated Ni_2P/$NiCr(OH)_2$-based HWE requires a small cell voltage of 0.513 V at 10 mA cm^{-2} and long-term stability for 800 h, which can efficiently upgrade sulfion into valuable elemental sulfur, achieving efficient H_2 production and resource utilization of sulfur pollution at low energy consumption.

Results and discussion

Synthesis and characterization

The synthesis route of Ni_2P/$NiCr(OH)_2$ is illustrated in Fig. 1a. A two-step hydrothermal reaction is employed to achieve uniform growth of the $Ni(OH)_2$/$NiCr(OH)_2$ precursor on NF, forming

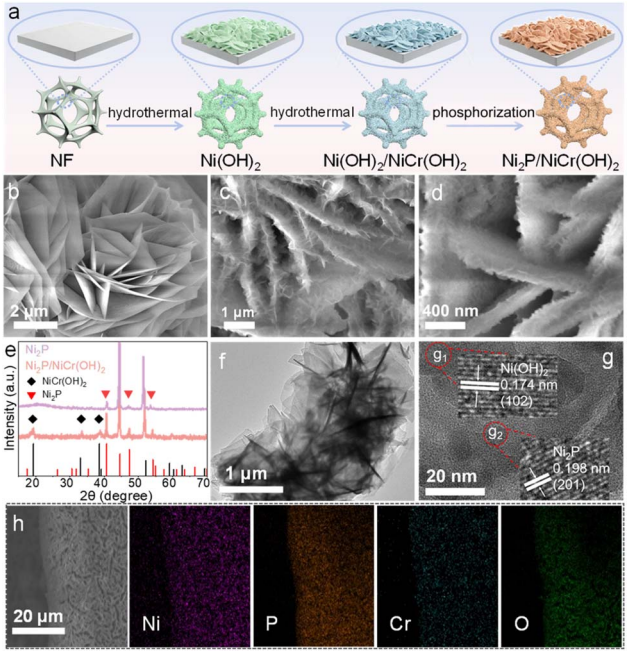

Fig. 1 (a) Schematic illustration of the synthesis process of Ni_2P/$NiCr(OH)_2$. SEM images of (b) $Ni(OH)_2$, (c) $Ni(OH)_2$/$NiCr(OH)_2$ and (d) Ni_2P/$NiCr(OH)_2$. (e) XRD patterns, (f) TEM image, (g) HRTEM image and (h) elemental mapping images of Ni_2P/$NiCr(OH)_2$.

a nanosheet-like structure. The surface morphology of $Ni(OH)_2$ is characterized using scanning electron microscopy (SEM). As displayed in Fig. 1b and S1a, the $Ni(OH)_2$ product shows a smooth nanosheet structure. In contrast, $Ni(OH)_2$/$NiCr(OH)_2$ exhibits a hierarchical nanosheet structure after the second hydrothermal reaction (Fig. 1c and S1d), where small nanosheets grow on the original $Ni(OH)_2$ nanosheets, implying the increased specific surface area.[37] Subsequently, the target Ni_2P/$NiCr(OH)_2$ precursor is obtained through the phosphorization process. SEM images (Fig. 1d and S1c) show that Ni_2P/$NiCr(OH)_2$ preserves a similar hierarchical nanosheet structure to the precursor without obvious structural alteration. The X-ray diffraction (XRD) patterns of Ni_2P and Ni_2P/$NiCr(OH)_2$ show that characteristic diffraction peaks can be well indexed to Ni_2P (PDF#74-1385) and $Ni(OH)_2$ (PDF#14-0117), confirming the formation of Ni_2P and Ni_2P/$NiCr(OH)_2$ (Fig. 1e). The transmission electron microscopy (TEM) image in Fig. 1f further verifies the layered nanosheet structure. In the high-resolution TEM (HRTEM) image (Fig. 1g), distinct lattice fringes with lattice spacings of 0.174 and 0.198 nm correspond to the (102) plane of $Ni(OH)_2$ and the (201) plane of Ni_2P, respectively. In Fig. S2, the mass ratio of Ni : P : Cr : O in Ni_2P/$NiCr(OH)_2$ is calculated to be 38.8 : 27.0 : 3.8 : 26.3, which is close to the Ni : Cr feeding ratio. Elemental mapping images of Ni_2P/$NiCr(OH)_2$ (Fig. 1h) confirm the coexistence and homogeneous distribution of Ni, P, Cr and O elements.

X-ray photoelectron spectroscopy (XPS) was employed to further investigate the surface chemical composition and elemental valence states of Ni_2P and Ni_2P/$NiCr(OH)_2$ catalysts. The survey XPS spectrum of Ni_2P/$NiCr(OH)_2$ (Fig. 2a) confirms

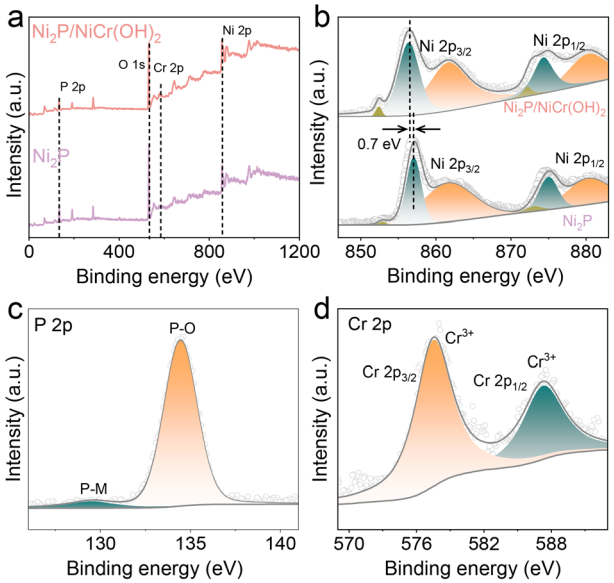

Fig. 2 (a) XPS spectra and (b) Ni 2p XPS spectra of Ni_2P and Ni_2P/$NiCr(OH)_2$. (c) P 2p XPS spectrum and (d) Cr 2p XPS spectrum of Ni_2P/$NiCr(OH)_2$.

the coexistence of Ni, P, Cr, and O elements, which is in good agreement with the elemental mapping results. While pristine Ni_2P shows characteristic peaks of Ni 2p, P 2p and O 1s, the emerged Cr 2p signal in the Ni_2P/$NiCr(OH)_2$ confirms successful incorporation of Cr. In Fig. 2b, the Ni 2p spectrum of Ni_2P displays two pairs of spin–orbit peaks at 852.4, 856.4 eV, and 872.7, 874.8 eV, belonging to Ni $2p_{3/2}$ and Ni $2p_{1/2}$, respectively. The additional peaks located at 861.6 and 880.2 eV correspond to satellite peaks.[38–40] After coupling with $NiCr(OH)_2$, the Ni 2p spectrum of Ni_2P/$NiCr(OH)_2$ reveals a negative shift of 0.7 eV compared with Ni_2P, indicating that the electronic structure optimization of Ni_2P and the presence of electronic interaction between Ni_2P and $NiCr(OH)_2$, which are beneficial to improve catalytic performances.[41,42] The P 2p XPS spectrum (Fig. 2c) demonstrates that the characteristic peak at 129.5 eV is associated with the phosphorus–metal (P–M) bonding configuration, confirming the successful fabrication of Ni_2P. The broad characteristic peak at 133.8 eV indicates the presence of P–O species on the sample surface, which originates from surface oxidation.[43,44] In the high-resolution Cr 2p XPS spectrum (Fig. 2d), two characteristic peaks are observed at binding energies of 587.3 and 577.5 eV, which correspond to the Cr $2p_{1/2}$ and Cr $2p_{3/2}$ states, respectively. The characteristic peak of Cr $2p_{3/2}$ at 577.5 eV corresponds to Cr^{3+}, which can modulate the electronic structure and surface active sites, playing a pivotal role in enhancing catalytic performance.[45–47] The O 1s spectrum in Fig. S3 reveals the presence of lattice oxygen at 530.9 eV, deficient oxygen at 531.8 eV, and adsorbed oxygen species at 533.3 eV.[48,49]

Electrochemical performances

The electrocatalytic performances of Ni_2P and Ni_2P/$NiCr(OH)_2$ catalysts toward the HER were evaluated in a three-electrode system. As shown in Fig. 3a and f, the catalytic activities are compared based on linear sweep voltammetry (LSV). The Ni_2P/

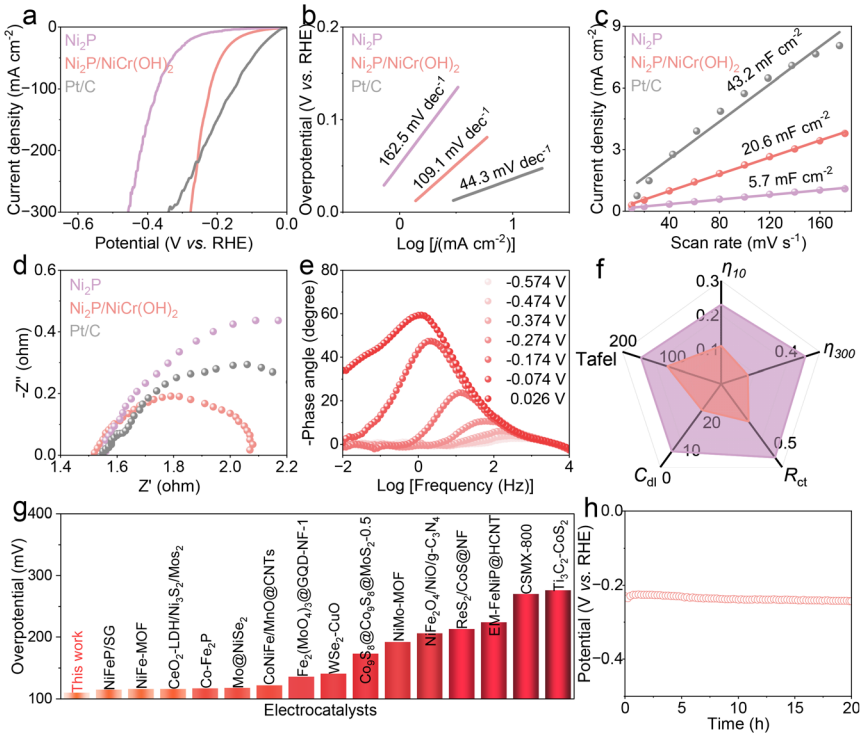

Fig. 3 (a) Polarization curves, (b) Tafel slopes, (c) C_{dl} calculation, and (d) EIS plots of different electrocatalysts. (e) Bode phase plots of Ni_2P/$NiCr(OH)_2$. (f) Radar chart and (g) overpotential comparison. (h) Long-term durability of Ni_2P/$NiCr(OH)_2$.

$NiCr(OH)_2$ requires a low overpotential of 0.111 V to reach a current density of 10 mA cm^{-2}, whereas Ni_2P needs a high value of 0.230 V, indicating its relatively inferior catalytic activity. The HER performance of $Ni_2P/NiCr(OH)_2$ is outstanding and superior to that of most reported catalysts, as summarized in Fig. 3g and Table S1. When the current density increases to 300 mA cm^{-2}, the required overpotential of $Ni_2P/NiCr(OH)_2$ is as low as 0.281 V, considerably lower than that of Ni_2P (0.456 V) and Pt/C (0.340 V). To further investigate the reaction kinetics, Tafel plots derived from corresponding LSV curves were analyzed. As shown in Fig. 3b and f, the Tafel slope of $Ni_2P/NiCr(OH)_2$ is 109.1 mV dec^{-1}, lower than that of Ni_2P (162.5 mV dec^{-1}), demonstrating that $NiCr(OH)_2$ incorporation can remarkably accelerate catalytic kinetics and achieve high current densities at low overpotentials. The double-layer capacitance values (C_{dl}) were calculated from cyclic voltammetry (CV) curves in the non-faradaic region (Fig. S4) to obtain the electrochemical active surface area (ECSA). As shown in Fig. 3c and f, the C_{dl} value of $Ni_2P/NiCr(OH)_2$ is 20.6 mF cm^{-2}, significantly larger than that of Ni_2P (5.7 mF cm^{-2}), suggesting abundant active sites and high intrinsic activity of $Ni_2P/NiCr(OH)_2$. To probe the electrode interfacial properties and charge transfer kinetics, electrochemical impedance spectroscopy (EIS) measurements were conducted. As presented in Fig. 3d and f, the charge transfer resistance (R_{ct}) of $Ni_2P/NiCr(OH)_2$ is calculated to be 0.27 Ω, which is smaller than that of Ni_2P (0.53 Ω), confirming that $NiCr(OH)_2$ introduction is beneficial to reduce charge transfer resistance, accelerate charge transfer and deliver superior electrocatalytic activity. In addition, *in situ* Bode plots (Fig. 3e and S5) indicate that $Ni_2P/NiCr(OH)_2$ possesses strong capacitive behavior and efficient HER charge transfer kinetics in the high-frequency region. The above results indicate that $NiCr(OH)_2$ introduction plays a crucial role in enhancing HER performances. The long-term stability of a catalyst is a key indicator for practical application. The stability test result in Fig. 3h shows that required potentials of $Ni_2P/NiCr(OH)_2$ remain nearly unchanged after continuous operation for 20 h. After the stability test, the SEM image of $Ni_2P/NiCr(OH)_2$ (Fig. S6) shows that there is no significant change in surface morphology, verifying its excellent structural stability.

The OER performances of $Ni_2P/NiCr(OH)_2$ were further evaluated. As shown in Fig. 4a and f, $Ni_2P/NiCr(OH)_2$ exhibits excellent OER activity with small potentials of 1.542 and 1.564 V at 60 and 300 mA cm^{-2}, respectively, lower than those of Ni_2P (1.563 and 1.608 V, respectively) and commercial RuO_2 (1.680 and 1.878 V, respectively). Moreover, the C_{dl} value of $Ni_2P/NiCr(OH)_2$ (Fig. S7) is higher than that of Ni_2P, indicating that $Ni_2P/NiCr(OH)_2$ can expose more catalytically active sites. Considering that the high inherent potential of the OER leads to significant increased energy consumption, the thermodynamically favorable SOR was further explored in 1 M NaOH and 1 M Na_2S. As shown in Fig. 4b and f, $Ni_2P/NiCr(OH)_2$ displays outstanding SOR activities with small voltages to achieve current densities of 10 and 300 mA cm^{-2} at 0.292 and 0.401 V, respectively, obviously lower than those of Ni_2P (0.361 and 0.785 V, respectively), indicating that the introduction of $NiCr(OH)_2$ can effectively regulate the surface electronic structure of Ni_2P

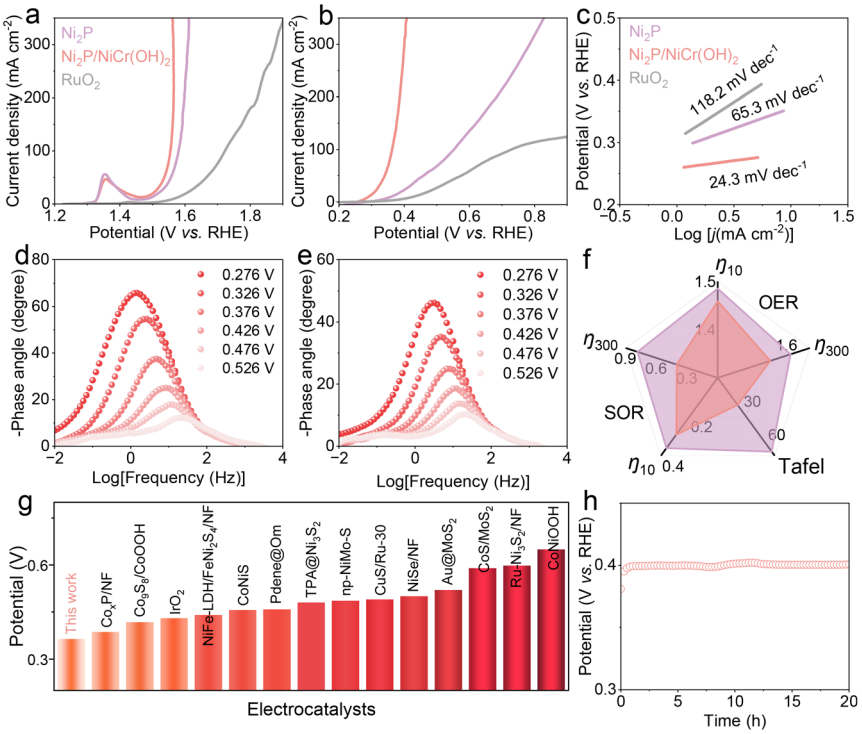

Fig. 4 (a) LSV curves for the OER. (b) LSV curves and (c) Tafel slopes for the SOR. Bode plots (d) of Ni_2P and (e) $Ni_2P/NiCr(OH)_2$. (f) Performance comparison of Ni_2P and $Ni_2P/NiCr(OH)_2$. (g) Overpotential comparison of developed catalysts and $Ni_2P/NiCr(OH)_2$. (h) Stability measurement for the SOR.

and significantly enhance SOR activity. The required potential for $Ni_2P/NiCr(OH)_2$ is lower than that of other previously developed catalysts (Fig. 4g and Table S2), fully demonstrating its performance advantage in electrocatalytic reactions. To analyze the SOR kinetic advantage of $Ni_2P/NiCr(OH)_2$, the Tafel curves were fitted and systematically analyzed. As shown in Fig. 4c and f, the Tafel slope of $Ni_2P/NiCr(OH)_2$ is 24.3 mV dec^{-1}, which is much smaller than those of Ni_2P (65.3 mV dec^{-1}) and commercial RuO_2 (118.2 mV dec^{-1}), further implying that $Ni_2P/NiCr(OH)_2$ has fast SOR kinetics, which can guarantee the efficient progress of the SOR. To reveal the intrinsic mechanism of the OER and SOR, Bode plots were used to analyze reaction kinetic processes of Ni_2P and $Ni_2P/NiCr(OH)_2$ at different potentials. As shown in Fig. 4d, e and S8, the phase angle of $Ni_2P/NiCr(OH)_2$ is significantly smaller than that of Ni_2P in the low-frequency range, indicating that $Ni_2P/NiCr(OH)_2$ has fast electron transfer rate and reaction kinetics during the OER and SOR. Notably, when the potential increases to 1.501 V, the phase angles of both Ni_2P and $Ni_2P/NiCr(OH)_2$ decrease sharply, indicating that a violent OER occurs, which is in agreement with previous results. As shown in Fig. 4f and S9, the potentials of $Ni_2P/NiCr(OH)_2$ remain nearly stable after continuous operation of 20 h under SOR and OER conditions, respectively. The post-test SEM images (Fig. S10 and S11) reveal that the nanosheet morphology of $Ni_2P/NiCr(OH)_2$ is well preserved, demonstrating its outstanding SOR and OER stabilities.

Given excellent bifunctional performances of $Ni_2P/NiCr(OH)_2$, the $Ni_2P/NiCr(OH)_2$-based flow electrolyzer (Fig. 5a) was integrated to verify its practical application, which employs a proton exchange membrane to separate the cathode and anode chambers, enabling efficient isolation and ion transport of cathodic and anodic reactions. As shown in Fig. 5b, the needed voltages of the HWE system are significantly lower than those of the OWS system at the same current density, confirming that replacing the OER with the SOR can effectively reduce energy input and achieve energy-saving H_2 production. Specifically, the required voltages of HWE are only 0.513 and 0.698 V to attain 10 and 100 mA cm^{-2}, respectively, much lower than those required in the OWS system (1.647 and 1.876 V, respectively) and many previously reported catalysts (Fig. 5d and Table S3). Meanwhile, $Ni_2P/NiCr(OH)_2$ shows much better electrocatalytic performance than Ni_2P, where $NiCr(OH)_2$ effectively boosts charge transfer and optimizes the surface structure. The long-term durability test of the $Ni_2P/NiCr(OH)_2$-based electrolyzer was performed. As shown in Fig. 5c, the HWE system driven by $Ni_2P/NiCr(OH)_2$ can ensure stable operation for up to 800 h with negligible voltage variation at 200 mA cm^{-2}. Furthermore, the post-test SEM image (Fig. S12) reveals that its structure remains largely intact, fully confirming its excellent durability. After the durability test, post-treatment and characterization were performed by adding sulfuric acid into the anodic electrolyte to gain a yellow powder product, which is verified as elemental sulfur (S_8, PDF#77-0145, Fig. S13). The above results indicate that the $Ni_2P/NiCr(OH)_2$-based HWE can achieve efficient conversion of sulfur-containing species into high-value-added elemental sulfur. To further confirm the impact of $NiCr(OH)_2$ introduction on catalytic performances of Ni_2P, *in situ* dark-field optical microscopy (DFLM) of Ni_2P and $Ni_2P/NiCr(OH)_2$ was carried out.[50–52] As shown in Fig. 5e and f, the H_2 bubble begins to generate on the surface of $Ni_2P/$

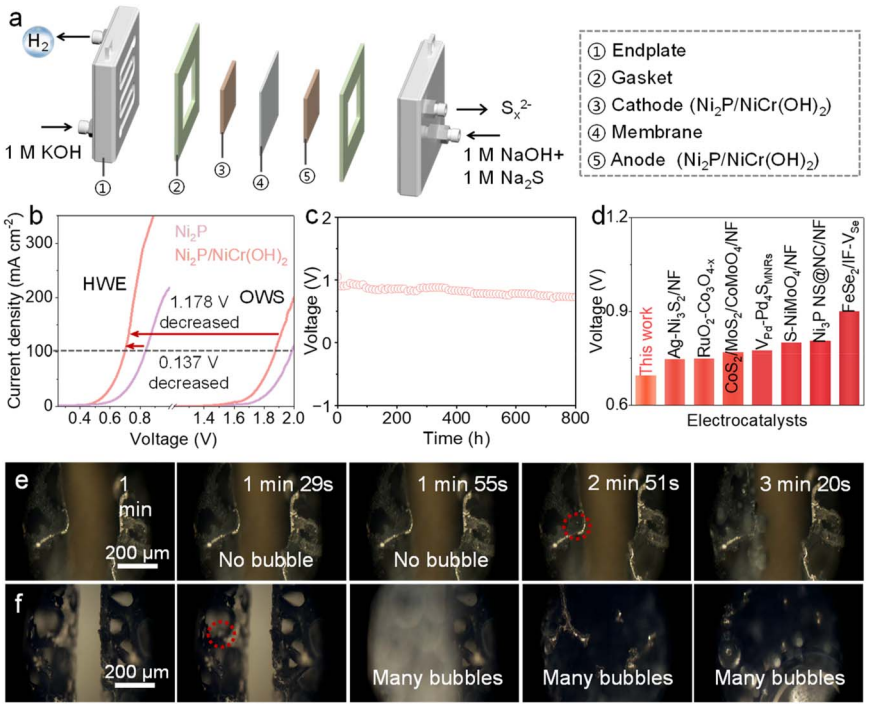

Fig. 5 (a) Schematic illustration of the assembled two-electrode HWE electrolyzer. (b) Polarization curves of HWE and OWS systems. (c) Durability tests of $Ni_2P/NiCr(OH)_2$ for the HWE system. (d) Voltage comparison of developed catalysts and $Ni_2P/NiCr(OH)_2$ for HWE systems. The time-lapse DFLM images of (e) Ni_2P and (f) $Ni_2P/NiCr(OH)_2$.

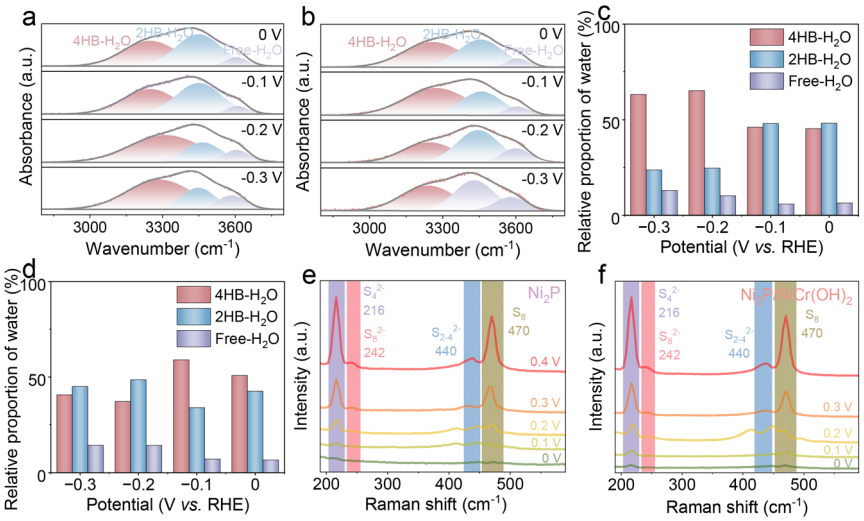

Fig. 6 Potential-dependent *in situ* ATR-FTIR spectra of the O–H stretching mode of interfacial water on the (a) Ni_2P and (b) $Ni_2P/NiCr(OH)_2$ electrocatalyst surface. The proportions of different types of water for (c) Ni_2P and (d) $Ni_2P/NiCr(OH)_2$. *In situ* Raman spectra of the electrolytes of (e) Ni_2P and (f) $Ni_2P/NiCr(OH)_2$ at various potentials in 1.0 M NaOH with 1 M Na_2S solution.

$NiCr(OH)_2$ at 1 min 29 s, while no gas bubble is observed on the surface of Ni_2P. Obvious and intensive gas bubbles occur on $Ni_2P/NiCr(OH)_2$ at 1 min 55 s, whereas the surface of Ni_2P still does not show any phenomenon of gas generation until 2 min 52 s and a large number of H_2 bubbles begin to form in Ni_2P at 3 min 20 s. These results directly demonstrate that $Ni_2P/NiCr(OH)_2$ possesses a higher catalytic performance and more intense electrochemical reaction process than Ni_2P. Therefore, the $Ni_2P/NiCr(OH)_2$-based HWE by coupling the HER and SOR not only effectively reduces overall electrolysis voltages, but also simultaneously realizes the high-value conversion of sulfur-containing wastewater into valuable elemental sulfur.

The *in situ* Raman spectroscopy of Ni_2P and $Ni_2P/NiCr(OH)_2$ was performed to analyze the catalytic process of the HER and SOR in 1.0 M NaOH without and with 1.0 M Na_2S electrolyte. For the HER, the interfacial water structures are analyzed (Fig. 6a and b), and the broad O–H stretching band (2800–3800 cm^{-1}) is deconvolved into three Gaussian peaks located at 3250 cm^{-1}, 3420 cm^{-1}, and 3590 cm^{-1}, which correspond to 4-coordinated H-bond water (4HB-H_2O), 2-coordinated H-bond water (2HB-H_2O), and the dangling O–H bonds of interfacial water (free-H_2O), respectively.[53] As we know, as the hydrogen-bond density among interfacial H_2O molecules increases, the corresponding O–H stretching vibration energy reduces, indicating that interfacial H_2O molecules with fewer hydrogen bonds are more easily dissociated. Consequently, the activation energy barrier for interfacial H_2O dissociation follows the order: free-H_2O < 2HB-H_2O < 4HB-H_2O. As shown n Fig. 6c and d, $Ni_2P/NiCr(OH)_2$ has a higher proportion of free-H_2O compared with Ni_2P, indicating that the enriched free H_2O at the $Ni_2P/NiCr(OH)_2$ interface favors catalytic performance.[54] These results show that the $NiCr(OH)_2$ introduction can restructure the interfacial water structure and weaken the hydrogen-bond network, which are beneficial to H_2O molecule mobility and reorientation, thus accelerating H_2O dissociation to form hydrogen intermediates, thus remarkably enhancing the HER activity.[55] For the SOR process, as the potentials gradually increase new characteristic peaks gradually appear at 216, 242, 440 and 470 cm^{-1} on the surface of Ni_2P and $Ni_2P/NiCr(OH)_2$, which belong to S_4^{2-}, S_8^{2-}, S_{2-4}^{2-} and S_8, respectively (Fig. 6e and f). These results confirm that a strong SOR response occurs and the S^{2-} gradually oxidizes to generate the short-chain polysulfur intermediates (S_x^{2-}), which eventually form S_8 molecules. However, the Raman characteristic peaks of Ni_2P are weaker compared to those of $Ni_2P/NiCr(OH)_2$ (Fig. 6e and f) with increasing potentials, indicating that the introduction of $NiCr(OH)_2$ effectively promotes the conversion of S^{2-} to polysulfide and elemental S_8.[56,57] These results verify that $Ni_2P/NiCr(OH)_2$ has better adsorption and conversion capacities in terms of polysulfide ions than Ni_2P, which effectively facilitates the SOR performance.

Conclusions

In summary, $Ni_2P/NiCr(OH)_2$ nanosheets were successfully fabricated *via* a two-step hydrothermal and phosphorization route. $Ni_2P/NiCr(OH)_2$ exhibits superior bifunctional activities for the HER and SOR, which deliver 10 mA cm^{-2} at 111 mV and 292 mV, respectively. *In situ* Raman spectroscopy and DFLM confirm that $NiCr(OH)_2$ incorporation can reorganize the interfacial water structure and boost reaction kinetics. The assembled electrolyzer exhibits ultra-long stability for 800 h and enables high current densities at low voltages, obviously lower than those required for traditional water electrolysis. This study provides a strategy to modulate the interfacial water structure and achieve energy-saving hydrogen production and resource utilization of sulfion-rich wastewater.

Author contributions

Xiaojun Wang: data curation and formal analysis. Jieting Li: investigation. Xinyu Zhu: formal analysis. Zehua Xu:

investigation. Shuixiang Xie: data curation. Shutong Chen: formal analysis. Yuxuan Wan: data curation. Guangyu Zhang: investigation. Mingzheng Ge: investigation. Wei Zhang: investigation. Chao Wang: conceptualization & investigation. Rui-Qing Li: conceptualization, writing – review & editing.

Conflicts of interest

There are no conflicts to declare.

Data availability

The relevant experimental and characterization data are available in the article and the supplementary information (SI). Supplementary information: the relevant experimental and characterization data including SEM images, XPS spectrum, CV curves, Bode plots C_{dl} values. See DOI: https://doi.org/10.1039/d6sc02309f.

Acknowledgements

This research was supported by the National Natural Science Foundation of China (No. 22302103), the Natural Science Foundation of Jiangsu Province (No. BK20230619), the Natural Science Foundation of the Jiangsu Higher Education Institutions of China (No. 23KJB540003), the Postgraduate Research & Practice Innovation Program of Jiangsu Province (No. KYCX25_3762), the National-Level Innovative Training Program Project for College Students of Nantong University (No. 202510304048), and Nantong University Analysis & Testing Center for SEM Characterization.

Notes and references

1 K. Modi, P. Pataniya, S. Siraj, P. Sahatiya, V. Patel and C. Sumesh, *J. Energy Storage*, 2023, **63**, 107040.
2 R. Li, X. Xu, J. Zeng, X. Zhang, X. Wan, S. Guo, X. Wang, S. Xie, Z. Cao, Y. Zhang, C. Wang, J. Deng, O. Fontaine, M. Ge, J. Dai, G. Zhang, W. Zhang, X. Wang and Y. Zhu, *Nano Lett.*, 2025, **25**, 1272.
3 J. Masnica, S. Sibt-e-Hassan, S. Potgieter-Vermaak, Y. Regmi, L. King and L. Tosheva, *Green Carbon*, 2023, **1**, 160.
4 X. Zhang, Y. Chen, Z. Ye, H. Hu, L. Lei, F. You, J. Yao, H. Yang and X. Jiang, *Chin. J. Struct. Chem.*, 2024, **43**, 100200.
5 S. Chauhan, K. Joshi, P. Pataniya and C. Sumesh, *Sustainable Energy Fuels*, 2025, **9**, 3550.
6 J. Liu, Y. Liu, B. Nan, D. Wang, C. Allen, Z. Gong, G. He, K. Fu, G. Ye and H. Fei, *Angew. Chem., Int. Ed.*, 2025, **64**, e202425196.
7 W. Song, J. Wu, J. Li, Z. Wang, T. He, W. Chen, D. Sun and J. Wu, *Green Carbon*, 2024, **2**, 393.
8 S. Xie, X. Zhu, Y. Zhang, F. Zhang, W. Fan, Z. Yang, G. Zhang, M. Ge, W. Zhang and R. Li, *Chem. Commun.*, 2026, **62**, 1641.
9 Y. Cheng, Y. wang, Z. Shi, H. Wu, J. Yang, J. Ni, M. Yang, Z. Wang, M. Xiao, C. Liu and W. Xing, *EcoEnergy*, 2025, **3**, 131.
10 J. Liang, Z. Cai, X. He, Y. Luo, D. Zheng, S. Sun, Q. Liu, L. Li, W. Chu, S. Alfaifi, F. Luo, Y. Yao, B. Tang and X. Sun, *Chem*, 2024, **10**, 3067.
11 M. Song, X. Yang, C. Guo, S. Zhang, J. Ma and H. Gao, *EcoEnergy*, 2025, **3**, 470.
12 S. Dristy, M. Habib, M. Joni, M. Najibullah, R. Mandavkar, S. Lin and J. Lee, *Chin. J. Struct. Chem.*, 2025, **44**, 100747.
13 C. Wang, L. Zhu, X. Wang and M. Wu, *Green Carbon*, 2025, **3**, 225.
14 H. Tüysüz, *Acc. Chem. Res.*, 2024, **57**, 558.
15 Y. Chen, Y. Liu, L. Li, T. Sakthive, Z. Guo and Z. Dai, *Adv. Funct. Mater.*, 2024, **34**, 2406587.
16 S. Wang, Z. Geng, S. Bi, Y. Wang, Z. Gao, L. Jin and C. Zhang, *Green Energy Environ.*, 2024, **9**, 659.
17 Y. Wang, L. Chen, H. Zhang, M. Humayun, J. Duan, X. Xu, Y. Fu, M. Bououdina and C. Wang, *Green Chem.*, 2023, **25**, 8181.
18 H. Sun, W. Zhang, J. Li, Z. Li, X. Ao, K. Xue, K. Ostrikov, J. Tang and C. Wang, *Appl. Catal., B*, 2021, **284**, 119740.
19 R. L, X. Wang, S. Xie, S. Guo, Z. Cao, Z. Yan, W. Zhang and X. Wan, *Chem. Sci.*, 2025, **16**, 809.
20 X. Zhang, J. Wang, K. Zong, Z. Chen, X. Yang, L. Yang, X. Wang and Z. Chen, *Carbon Energy*, 2025, **7**, e679.
21 Y. Zhang, L. Liao, H. Zhou, Y. Qi, J. Sun, Y. Zhang, Q. Zhou, Y. Wang, D. Tang and F. Yu, *Energy Environ. Sci.*, 2025, **18**, 7695.
22 Y. Ramli, V. Chaerusani and Z. Yang, *Green Carbon*, 2025, **3**, 113.
23 Y. Zhang, H. Wang, J. Lee and Q. Zhang, *Chin. J. Catal.*, 2023, **55**, 44.
24 H. Thakkar, K. Modi, K. Joshi, G. Bhadu, S. Siraj, P. Sahatiya, P. Pataniya and C. Sumesh, *ACS Sustainable Chem. Eng.*, 2024, **12**, 8340.
25 R. Li, X. Wang, S. Xie, S. Guo, Z. Cao, Z. Yan, W. Zhang and X. Wan, *Chem. Sci.*, 2025, **16**, 809.
26 Y. Nie, X. Liu, J. Li, R. Wang and B. Dong, *Chem. Commun.*, 2026, **62**, 594.
27 L. Ai, Y. Tian, T. Xiao, J. Zhang, C. Zhang and J. Jiang, *J. Colloid Interface Sci.*, 2024, **673**, 607.
28 J. Huo, L. Jin, C. Chen, D. Chen, Z. Xu, C. Wilfred, Q. Xu and J. Lu, *ACS Appl. Mater. Interfaces*, 2023, **15**, 43976.
29 S. Xie, X. Wang, Y. Li, S. Liu, J. Qian, Y. Zhang, L. Jiang, Z. Cao, Z. Yan, X. Wan, Z. Yang, L. Zou, W. Zhang and R. Li, *Chem. Sci.*, 2025, **16**, 12587.
30 C. Duan, C. Tang, S. Yu, L. Li, J. Li and Y. Zhou, *Appl. Catal., B*, 2023, **324**, 122255.
31 H. Yang, X. Long, F. Liu, J. Zhou, N. Chen, R. Feng, Y. Zhang, X. Fu, J. Luo and B. Zhao, *Appl. Catal., B*, 2025, **366**, 125037.
32 X. Li, W. Yu, Y. Wang, R. Liu, Q. Yu, R. Hu, X. Jiang, Q. Gao, H. Liu, J. Yu and W. Zhou, *Chin. Chem. Lett.*, 2024, **35**, 109166.
33 S. Shi, M. Li, J. Zeng, J. Wang, G. Zeng and Q. Zhong, *J. Electroanal. Chem.*, 2025, **986**, 119076.
34 Z. Yu, D. Boukhvalov, H. Tan, D. Xiong, C. Feng, J. Wang, W. Wang, Y. Zhao, K. Xu, W. Su, X. Xiang, F. Lin, H. Huang, F. Zhang, L. Zhang, L. Meng and L. Liu, *Chem. Eng. J.*, 2024, **494**, 153094.

35 Z. Liang, Y. Nian, H. Du, P. Li, M. Wang and G. Ma, *Materials*, 2025, **18**, 3377.
36 H. Li, J. Ding, Z. Wei, L. Zhuo, I. Shakir, J. Deng, G. Hu and X. Liu, *Int. J. Hydrogen Energy*, 2026, **199**, 152878.
37 M. Koudahi and L. Naji, *Electrochim. Acta*, 2022, **434**, 141314.
38 M. Yang, J. Ding, Z. Wang, J. Zhang, Z. Peng and X. Liu, *Chin. Chem. Lett.*, 2025, **36**, 110861.
39 S. Liu, Y. Gu, J. Kang, J. Zhang, S. Liu, H. Yang, X. Zhu and M. Ming, *Int. J. Hydrogen Energy*, 2026, **198**, 152670.
40 S. Zhang, X. Yang, L. Ma, J. Ma and H. Gao, *Mater. Today Chem.*, 2025, **49**, 103095.
41 L. Wu, L. Yu, F. Zhang, B. McElhenny, D. Luo, A. Karim, S. Chen and Z. Ren, *Adv. Funct. Mater.*, 2021, **31**, 2006484.
42 H. Huo, H. Hou, Y. Yu, J. Xu, W. Chen, S. Wang and D. Min, *Electrochim. Acta*, 2025, **544**, 147697.
43 Z. Wang, G. Yang, P. Tian, X. Li, K. Deng, H. Yu, Y. Xu, H. Wang and L. Wang, *Chem. Eng. J.*, 2023, **473**, 145147.
44 J. Park, H. Yoon, D. Lee, S. Ji, W. Yang, S. Tilley, M. Sung, I. Park, J. Tan, H. Lee, J. Kim, D. Kim and J. Moon, *Appl. Catal., B*, 2022, **305**, 121045.
45 Y. Pei, D. Li, C. Qiu, L. Yan, Z. Li, Z. Yu, W. Fang, Y. Lu and B. Zhang, *Angew. Chem., Int. Ed.*, 2024, **136**, e202411977.
46 Y. Nie, H. Feng, H. Wang, Y. Hu, L. Cao and B. Dong, *Chem. Eng. J.*, 2025, **523**, 168370.
47 F. Sun, Y. Wang, H. Gao, X. Tian, R. Zhu, Y. Zheng, J. Zang and L. Dong, *Appl. Catal. B Environ.*, 2025, **383**, 126109.
48 R. Li, S. Guo, X. Wang, X. Wan, S. Xie, Y. Liu, C. Wang, G. Zhang, J. Cao, J. Dai, M. Ge and W. Zhang, *Chem. Sci.*, 2024, **15**, 10084.
49 Y. Dang, P. Düngen, J. Hao, X. Sun, Y. Ding and S. Heumann, *Green Carbon*, 2026, DOI: 10.1016/j.greenca.2025.10.009.
50 C. Wang, Q. Xie, G. Wang, Y. Lyu, Q. Wang, X. Ma, H. Wang, T. Guo, Y. Wu and J. Han, *Nano Lett.*, 2024, **24**, 13796.
51 C. Wang, H. Wang, X. Ma, T. Guo, A. Zheng, Y. Zhao, X. Li, Y. Wu, S. Li and J. Han, *Nano Lett.*, 2025, **25**, 6556.
52 N. Liu, G. Zhou, A. Yang, X. Yu, F. Shi, J. Sun, J. Zhang, B. Liu, C. Wu, X. Tao, Y. Sun, Y. Cui and S. Chu, *Proc. Natl. Acad. Sci. U. S. A.*, 2019, **116**, 765.
53 Z. Huang, Z. Chen, C. Xu, L. Wang, M. Gao, S. Zhang, T. Isimjan, X. Shi, Y. Ye, L. Chen, J. Wang, X. Yang, Y. Zhu and B. Wu, *Adv. Funct. Mater.*, 2026, e14861.
54 Y. Wan, Y. Tang, Y. Zuo, K. Sun, Z. Zhuang, Y. Zheng, W. Yan, J. Zhang and R. Lv, *Energy Environ. Sci.*, 2025, **18**, 7460.
55 J. Zhu, X. Sun, N. Feng, B. Zhao, M. Qiu, J. Xu and W. Luo, *J. Am. Chem. Soc.*, 2025, **147**, 47454.
56 Y. Nie, H. Feng, H. Wang, Y. Hu, L. Cao and B. Dong, *Chem. Eng. J.*, 2025, **523**, 168370.
57 C. Duan, C. Tang, S. Yu, L. Li, J. Li and Y. Zhou, *Appl. Catal., B*, 2023, **324**, 122255.